

Auxetic interval determination and experimental validation for a three-dimensional periodic framework

Borcea, Ciprian S.; Broeren, Freek G.J.; Herder, Just L.; Streinu, Ileana; van der Wijk, Volkert

DOI

[10.1177/10812865211041390](https://doi.org/10.1177/10812865211041390)

Publication date

2021

Document Version

Final published version

Published in

Mathematics and Mechanics of Solids

Citation (APA)

Borcea, C. S., Broeren, F. G. J., Herder, J. L., Streinu, I., & van der Wijk, V. (2021). Auxetic interval determination and experimental validation for a three-dimensional periodic framework. *Mathematics and Mechanics of Solids*, 27 (2022)(5), 764-774. <https://doi.org/10.1177/10812865211041390>

Important note

To cite this publication, please use the final published version (if applicable). Please check the document version above.

Copyright

Other than for strictly personal use, it is not permitted to download, forward or distribute the text or part of it, without the consent of the author(s) and/or copyright holder(s), unless the work is under an open content license such as Creative Commons.

Takedown policy

Please contact us and provide details if you believe this document breaches copyrights. We will remove access to the work immediately and investigate your claim.

Auxetic interval determination and experimental validation for a three-dimensional periodic framework

Ciprian S. Borcea 

Department of Mathematics, Rider University, Lawrenceville, NJ, USA

Freek G. J. Broeren 

*Department of Precision and Microsystems Engineering,
Delft University of Technology, Delft, the Netherlands*

Just L. Herder

*Department of Precision and Microsystems Engineering,
Delft University of Technology, Delft, the Netherlands*

Ileana Streinu

Computer Science Department, Smith College, Northampton, MA, USA

Volkert van der Wijk

*Department of Precision and Microsystems Engineering,
Delft University of Technology, Delft, the Netherlands*

Received 9 April 2021; accepted: 4 August 2021

Abstract

Auxetic behavior refers to lateral widening upon stretching or, in reverse, lateral shrinking upon compression. When an initially auxetic structure is actuated by compression or extension, it will not necessarily remain auxetic for larger deformations. In this paper, we investigate the auxetic range in the deformation of a periodic framework with one degree of freedom. We use geometric criteria to identify the interval where the deformation is auxetic and validate these theoretical findings with compression experiments on sample structures with $10 \times 10 \times 10$ unit cells.

Keywords

Auxetic interval, periodic framework, compression test

Corresponding author:

Freek Broeren, Department of Precision and Microsystems Engineering, Delft University of Technology, Room 34-G-I-120, Mekelweg 2, Delft, Zuid-Holland 2628CD, the Netherlands.
Email: f.g.j.broeren@tudelft.nl

Mathematics and Mechanics of Solids
2022, Vol. 27(5) 764–774
© The Author(s) 2021



Article reuse guidelines:
sagepub.com/journals-permissions
DOI: 10.1177/10812865211041390
journals.sagepub.com/home/mms



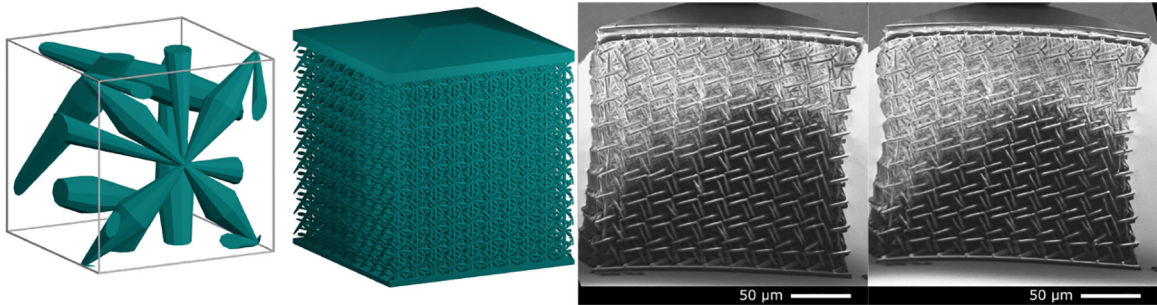


Figure 1. The framework used in compression experiments. Description and dimensions are given in the text. See also Figure 6

1. Introduction

Auxetic structures have the curious property that they shrink in all directions under uniaxial compression and widen in all directions under stretching. Early considerations on this type of behavior appeared in [1–4]. Foam structures reported by Lakes [5] kindled wider interests in cellular and periodic designs which exhibit *auxetic deformations* [6, 7]. The scope of investigations and proposed applications can be gleaned from a string of reviews [8–15]. Advances in additive manufacturing have permitted the fabrication of increasingly complex and intricate structures [16–20], leading to a renewed emphasis on rational design. As observed in [21], “the rational design of metamaterials with a target property or functionality remains fiendishly difficult, and many designs so far have relied on luck and intuition.”

In this paper, we focus on periodic bar-and-joint frameworks with auxetic behavior. Structures of this type, also referred to as a “rods and hinges lattices,” “metamaterials of rigid bars and pivots,” or simply “trusses,” have been frequently used in investigations concerned with the geometric underpinnings of auxetic deformations [22–26]. We note, in this context, that crystalline materials provide a vast array of periodic bar-and-joint frameworks, also called “crystal structures” or “crystal nets” [27–30]. Displacive phase transitions, occurring under variations of temperature or pressure, can oftentimes be modeled as periodic framework deformations [31–33] and inquiries about auxetic behavior have been conducted for various structures [34–37].

Materials which can be modeled as periodic bar-and-joint frameworks allow a direct comparison of theoretical predictions with experimental results, thereby offering a more precise understanding of the fundamental role of geometry in functional responses. For auxetic behavior, there is a strictly mathematical theory, developed in [38–40], which gives necessary and sufficient conditions for the existence of auxetic infinitesimal deformations and leads to a comprehensive design methodology. As auxetic behavior is necessarily confined to a limited range, these results bring to the fore the problem of identifying, in the global deformation space of a periodic framework, all regions where auxetic deformations are possible [41].

In the present study, we explore the long-range behavior of a three-dimensional periodic framework with one degree of freedom, introduced in [42]. Figure 1 illustrates the sample structure produced for experiments and an actual response recorded for compression. We determine the entire deformation path of the framework and recognize auxeticity along a limited arc of this trajectory. The auxetic interval of the framework is obtained through rigorous geometric calculations. The existence of this interval is then validated through experiments on 3D printed structures with $10 \times 10 \times 10$ unit cells measuring $200 \mu\text{m}$ in total side length. These structures are compressed and the lateral deformation is measured through computer vision.

In our concluding section, we elaborate on the significance of one-degree-of-freedom framework designs and the importance of the notion of auxetic interval, which allows a numerical comparison of auxetic performance for different frameworks in this class via the *volume increase factor* for the unit cells at the endpoints of the interval.

2. The periodic framework

The specific periodic framework considered here belongs to a family of designs presented in [42]. It is obtained from the diagram shown in Figure 2. On the left, we see a fragment of a cubic lattice consisting of 7 cubes inside a sphere passing through the 24 outlying corners. In the middle, the image shows an octet of lattice points chosen from these corners and connected by edges to an additional vertex placed on the sphere. This common vertex of the eight edges is chosen along the axis running through the center of the sphere and the

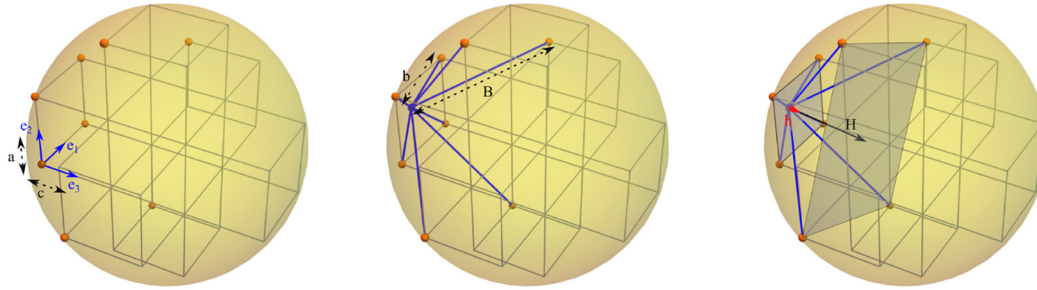


Figure 2. Design diagram of the periodic framework. The unit vectors e_1 , e_2 , and e_3 , forming an orthonormal basis, as well as the distances a , b , B , c , h , and H are indicated.

centers of the two squares determined by the octet of lattice points. This gives a rotational symmetry of order four to the generating configuration and we use the expression “four-fold symmetry” to refer to the resulting crystallographic symmetry of the periodic framework.

The periodicity lattice is $2\mathbb{Z}^3$, consisting of all vectors in Euclidean three-dimensional space with even integers as coordinates. Thus, the side length of the cubes depicted in the sphere is 2 and the radius of the sphere is $\sqrt{11}$. The four short edges have squared length $b^2 = 22 - 6\sqrt{11}$ and the four long edges have squared length $B^2 = 22 - 2\sqrt{11}$.

2.1. The global deformation space

The geometric model assumes all edges of the framework to be rigid bars and all joints to allow free relative rotation of the incident bars. The initial configuration of this periodic framework then has one degree of freedom and the deformation mechanism can be visualized and described by taking into account the preservation of the four-fold rotational symmetry. The vectors e_1, e_2, e_3 denote the standard orthonormal basis of our Euclidean three-dimensional space. The symmetry axis remains fixed along the e_3 direction and the one-parameter deformation is obtained by the variation of the periodicity lattice which keeps the direction of the initial periodicity generators $2e_1, 2e_2, 2e_3$ and keeps the first two generators of equal length. In other words, the initial cubic cell determined by the generators evolves into an orthogonal box which maintains square faces normal to the symmetry axis direction (e_3). We let a denote half the edge length of the square face and let c denote half the edge length of the third periodicity generator (with direction e_3). Thus, the initial configuration has $a = c = 1$.

When the framework moves along its deformation path, it suffices to describe what happens to the eight-bar configuration depicted in Figure 2. We observe that the common vertex remains along the fixed axis and the four ends of the short bars form a square of edge length $2a$ with center on the axis and normal to the axis. The four ends of the long bars are the vertices of a square with center on the axis, normal to the axis and the distance between the planes of these two squares is $2c$.

If we denote by h the distance of the common vertex to the center of the first square and by H the distance to the center of the second square, we have

$$h^2 = b^2 - 2a^2 \quad (1)$$

$$H^2 = B^2 - 10a^2 \quad (2)$$

We note that a is constrained to remain in the interval $(0, b/\sqrt{2}]$, because $0 \leq h^2 < b^2$. The relation between a and c depends on whether the common vertex is between the two squares or not (as in the initial configuration). Thus,

$$c = \frac{1}{2}(H \pm h) = \frac{1}{2}[\sqrt{B^2 - 10a^2} \pm \sqrt{b^2 - 2a^2}] \quad (3)$$

which implies the algebraic relation:

$$(4c^2 - 8a^2 + B^2 - b^2)^2 - 16c^2(B^2 - 10a^2) = 0 \quad (4)$$

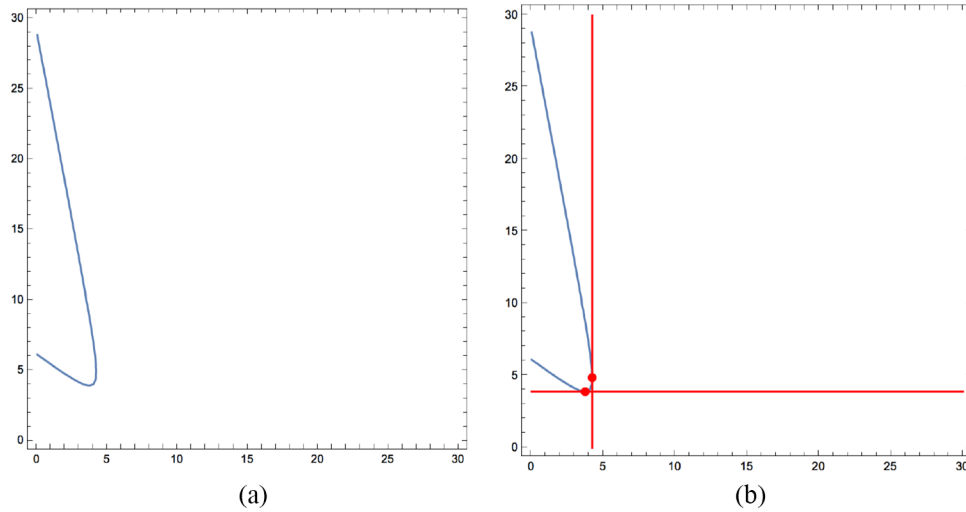


Figure 3. Gram matrix trajectory in $(\omega_{22}, \omega_{33})$ coordinates, with auxetic interval between points with horizontal and vertical tangent.

Considering that the Gram matrix ω for the periodicity generators is diagonal, with entries $\omega_{11} = \omega_{22} = 4a^2$ and $\omega_{33} = 4c^2$, we see via (4) that the Gram matrix trajectory is the arc of the conic

$$Q(\omega_{22}, \omega_{33}) = (\omega_{33} - 2\omega_{22} + B^2 - b^2)^2 - 2\omega_{33}(2B^2 - 5\omega_{22}) = 0 \tag{5}$$

where $\omega_{22}, \omega_{33} > 0$. This arc of a hyperbola is shown in Figure 3(a).

2.2. Geometrical determination of the auxetic interval

The detection of the precise interval where the deformation is auxetic will illustrate the geometric criteria established in [38, 39]. In particular, auxetic behavior requires, for all pairs of orthogonal directions, simultaneous elongation, or, under compression, simultaneous shrinking. Computationally, we have to see where a and c increase or decrease at the same time. As the derivative of $c(a)$ is negative when the common vertex is between the two squares, we are left with the alternative

$$c(a) = \frac{1}{2}(H - h) = \frac{1}{2}[\sqrt{B^2 - 10a^2} - \sqrt{b^2 - 2a^2}] \tag{6}$$

Figure 4 shows the graph of this function. We have

$$c'(a) = -5a(B^2 - 10a^2)^{-1/2} + a(b^2 - 2a^2)^{-1/2} = -\frac{5a}{H(a)} + \frac{a}{h(a)} \tag{7}$$

There is one critical point in $(0, b/\sqrt{2})$, namely

$$a_0 = \sqrt{\frac{1}{10}(132 - 37\sqrt{11})} \approx 0.963581 \tag{8}$$

and (7) is negative to the left and positive to the right of a_0 .

The *auxetic interval* is where $a \in [a_0, b/\sqrt{2}] \approx [0.963581, 1.02476]$ and c is given by (6). The (a, c) pairs at the endpoints are

$$\left(\sqrt{\frac{1}{10}(132 - 37\sqrt{11})}, 2\sqrt{\frac{1}{5}(7\sqrt{11} - 22)} \right) \approx (0.963581, 0.986458) \tag{9}$$

$$(\sqrt{11 - 3\sqrt{11}}, \sqrt{7\sqrt{11} - 22}) \approx (1.02476, 1.10289) \tag{10}$$

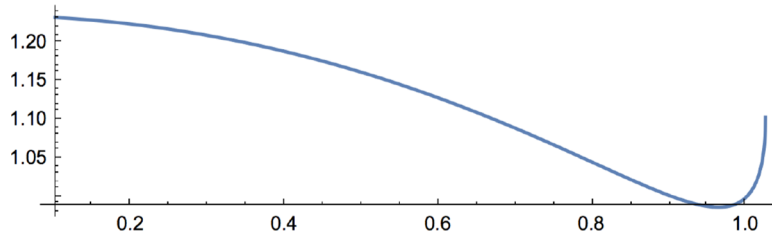


Figure 4. The graph of $c(a)$ in (6), for $a \in (0, 1.02476)$.

The auxetic interval can be retrieved based on the *directions of the tangents to the Gram matrix trajectory* given in (5) and shown in Figure 3. By [38], the auxetic locus is where the tangents have directions belonging to the *positive semidefinite cone* of 3×3 symmetric matrices. Our trajectory lies in the plane $\omega_{11} = \omega_{22}$, $\omega_{ij} = 0$, for $i \neq j$, whose intersection with the positive semidefinite cone corresponds with $\omega_{22}, \omega_{33} \geq 0$.

Thus, in Figure 3, the auxetic interval can be visualized as the *arc between the points of the trajectory where the tangent is horizontal and then vertical*. These points correspond to

$$\frac{\partial Q}{\partial \omega_{22}} = 0, \text{ respectively } \frac{\partial Q}{\partial \omega_{33}} = 0 \quad (11)$$

We find

$$3\omega_{33} = 2(B^2 - b^2) - 4\omega_{22}, \text{ respectively } \omega_{33} = B^2 + b^2 - 3\omega_{22} \quad (12)$$

and this determines the endpoints of the *auxetic interval* on the Gram matrix trajectory as

$$(\omega_{22}, \omega_{33}) = \left(\frac{2}{5}(132 - 37\sqrt{11}), \frac{16}{5}(7\sqrt{11} - 22) \right) \approx (3.71395, 3.8924) \quad (13)$$

$$(\omega_{22}, \omega_{33}) = (44 - 12\sqrt{11}, 28\sqrt{11} - 88) \approx (4.2005, 4.86549) \quad (14)$$

Figure 3 shows the auxetic arc of the trajectory between these two endpoints. The relation $(\omega_{22}, \omega_{33}) = (4a^2, 4c^2)$ allows an easy comparison with the (a, c) points in (9) and (10) and we conclude that our two descriptions of the auxetic window agree.

3. Experimental methods

3.1. Structure design

From the framework blueprint described previously, a monolithic design was created. The design process is illustrated in Figure 5.

To create a monolithic sample of the framework, each of the edges in the blueprint shown in Figure 2 is replaced by a bicone, as shown in Figure 5(a). By doing this, we obtain a fundamental unit consisting of eight bicones connected in a single point. We can then replicate this fundamental unit and translate it along the vectors of the periodicity lattice, as illustrated in Figure 5(b), to obtain the complete monolithic structure.

The monolithic structure was realized with edge lengths of $b = 14.5 \mu\text{m}$ for the short edges and $B = 39.2 \mu\text{m}$ for the long edges, resulting in $a = c = 20 \mu\text{m}$ in the initial configuration. The bicones that replace each of the edges have a small diameter of $0.5 \mu\text{m}$ at their ends and a large diameter in the middle of $4 \mu\text{m}$. The unit cell of the periodic framework was repeated 10 times along each of the periodicity generators to create a structure with 1000 unit cells in total, arranged into a cube. On the bottom of this cube, a plate with a thickness of $5 \mu\text{m}$ was placed to ensure a level surface, and on the top a flattened pyramid was placed. The resulting unit cell and the complete sample structure are shown in Figure 6.

3.2. Sample creation

All sample structures were manufactured using two-photon lithography on a Nanoscribe Photonic Professional GT (Nanoscribe GmbH, Eggenstein-Leopoldshafen, Germany), using IP-Dip photoresin on a silicon substrate.

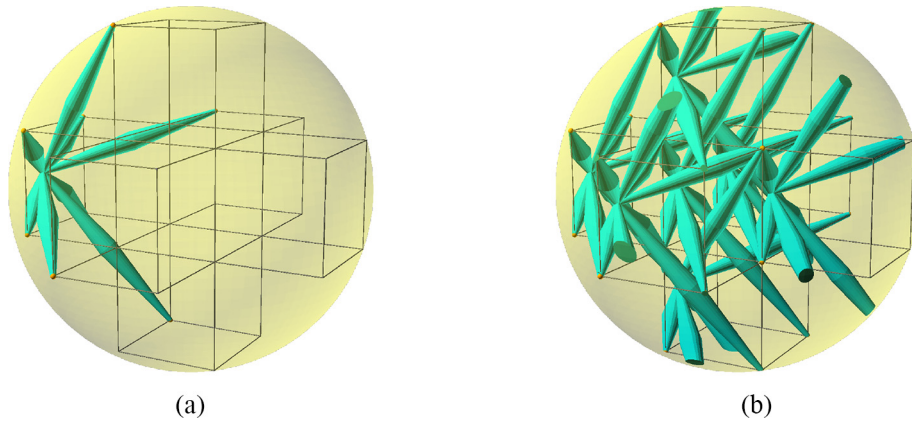


Figure 5. The monolithic implementation of the periodic framework is developed in two steps. (a) First, the edges in the blueprint of Figure 2 are replaced by bicones. (b) Second, the eight bicones that make up a fundamental unit are copied and translated along the vectors of the periodicity lattice to generate the periodic structure.

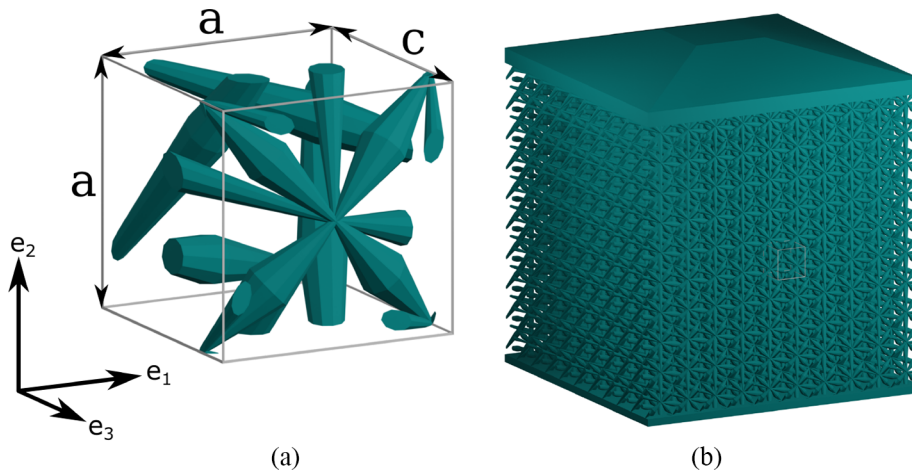


Figure 6. The designed periodic framework. (a) A single unit cell, with the unit cell volume outlined by gray lines. The dimensions a and c are indicated along the corresponding sides of the cubic unit cell and the corresponding unit vectors e_i are indicated separately. (b) The complete 1000 unit cell structure, with a plate on the bottom for adhesion and a shallow pyramid on the top for probe alignment.

This machine is capable of a lateral resolution of 200 nm and can create structures up to 400 μm high. The printed structures were sputter-coated with approximately 4 nm of gold–palladium in order to image them in a scanning electron microscope (SEM).

After creating and testing the structures, it was observed that the plates on the top and bottom of the structures appear slightly curved and the central part of the structure is already slightly narrower than the top and bottom parts. This is likely an effect of the shrinkage of the used resin, which is reported to be up to 10% (see [43]). As we describe in Section 3.4, a central region of the structure is measured to decrease the effect of these boundaries.

3.3. Sample testing

Two uniaxial load cases are considered. One where a uniaxial deformation is applied along the four-fold symmetry axis, i.e., along direction e_3 . In this case, c is the driving parameter. For this load case, the four viewing directions normal to the faces are equivalent and the lateral deformation of a can be measured as a response to a deformation in c .

In the other load case, the structure is uniaxially deformed along direction e_2 , perpendicular to the symmetry axis and a is the driving parameter. There are two distinct side-views for this case, one along e_3 , where we view

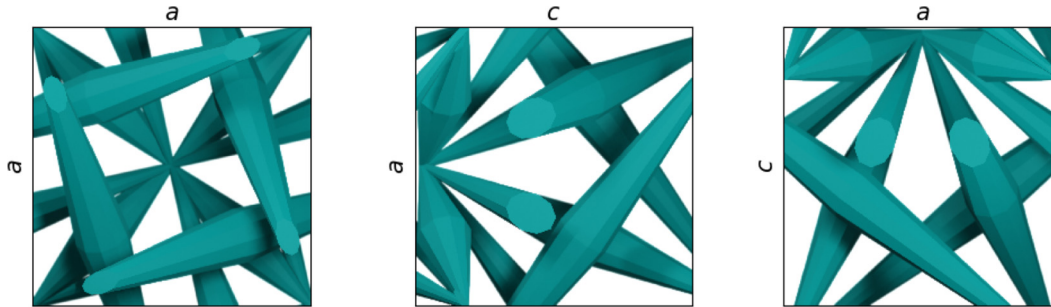


Figure 7. Schematics of the three distinct viewing directions of the structure that are used in this study. The images show an orthographic view of a single unit cell of structure and the relevant dimensions a and c are marked on the sides of the images.

the deformation of the second side marked a under compression and one along e_1 , where the deformation in c is visible.

Three structures were constructed, one for each testing orientation. The two structures to be compressed along e_2 were constructed identically, with the only difference being a 90° rotation of the complete structure (including plates) along the axis normal to the substrate.

The structures were compressed using a Femtotools FT-NMT03 nanomechanical testing system inside of a Jeol JSM-6010LA SEM. For the compression tests, a silicon microforce sensing probe with a tip width of $50\ \mu\text{m}$ was used. The probe was centered on the structures by aligning it with the flattened pyramid. The structures were compressed at a rate of $0.1\ \mu\text{m s}^{-1}$. Every $0.2\ \mu\text{m}$ of travel, the probe was stopped and the SEM was used to record a high-resolution (5120×3840 pixels) image. Each compression step corresponds to 0.1% of applied strain to the structure.

3.4. Experimental probing of the auxetic interval

Owing to the four-fold rotational symmetry described in Section 2, the auxetic interval can be determined by measuring the effects of applied deformations on the distances a and c . For each compression test, the structure is imaged from the side, allowing two dimensions to be measured during the deformation, one of which is always the driving parameter.

Figure 7 shows a unit cell of the framework under the three different viewing directions. The distance labels a and c can be seen next to the respective sides of the frames.

We observe that, according to Figure 4, when a is actuated, the allowed compression is relatively large, whereas when c is actuated, the allowed compression of the sample is limited to about 1.35%. Up to this limit, a point on the motion path corresponding to this compression can be found. Beyond this limit, no such point can be found and the framework can therefore no longer respect the intended structural design. In experiments, this will result in deformations which significantly or severely violate the rigid-bar assumption. Therefore, when probing the auxetic interval experimentally, applied strains larger than 1.35% along c do not reflect the theoretical structure in a meaningful way. In our test, we have compressed the structure slightly further to ensure that the full range of motion was measured in the selected region, considering that the deformations are not distributed equally throughout the structure.

3.5. Data processing

The recorded images were used to obtain quantitative data on the strains in the compressed structures. First, the images were rotated and straightened to correct for perspective. To do this, four points on the structure were selected and transformed to span a square.

The images were then processed using digital image correlation. The deformations were tracked in a central region of the structure, consisting of 6×4 unit cells, to mitigate the effects of the boundaries. This region was tracked using Gunnar Farneback's algorithm, as implemented in OpenCV 3.2.0 [44, 45]. Using this algorithm, the displacements of each pixel in the region are calculated. We use these displacements to calculate the local strains in the tracked region and average this over the region to obtain the horizontal and vertical strains.

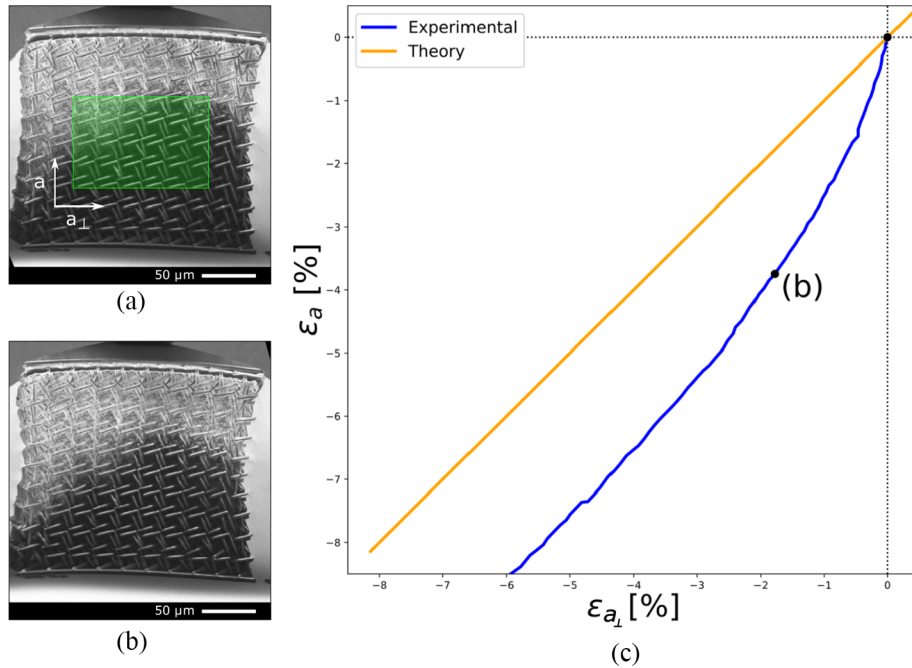


Figure 8. Strains and images from a compression test along the e_2 direction, measuring the orthogonal strain along a_{\perp} , with vertical dimension a as the driving parameter. (a) The undeformed state of the structure. The analyzed region is highlighted in green and the directions a and a_{\perp} are indicated. (b) The deformed state at the end of the calculated auxetic interval.

4. Results

Compression tests were performed on the structures for each of the three distinct viewing directions. For each test, the resulting horizontal and vertical strains were recorded. In the following figures, we report the engineering strains:

$$\epsilon_x = \frac{x - x_0}{x_0} \quad (15)$$

where x is the dimension under study and x_0 is its initial length. Note that we can obtain these strains from the distances a and c from Section 2.2 by subtracting 1, because these distances have an original size of 1. We discuss each viewing direction separately. We present these strains from both experiment and theory. Next to the plots, we show the state of the structure at the initial position and at the theoretical end of the auxetic interval. These positions are labeled (a) and (b), respectively, in the figures.

The results of the first experiment are shown in Figure 8. Here, the structure was compressed along the e_2 direction, with a as the driving parameter and the perpendicular a direction (denoted by a_{\perp}) as the orthogonal direction under study. The plot in the figure shows the strains observed in the experiment as well as the strains determined from theory. In the calculated and the experimentally obtained curve, both strains are continuously decreasing throughout the experiment. However, in the experiment, we see that the orthogonal strain lags behind the theoretical value.

Figure 9 shows the results of the experiment where the structure was compressed along the e_2 direction, making a the driving parameter, and c the orthogonal direction under study. In both the theoretical strains and the experimental strains, we see that there is a minimum for ϵ_c , after which this orthogonal strain increases again for continuing compression. In the theoretical curve, this minimum occurs at $\epsilon_a = -3.7\%$, $\epsilon_c = -1.35\%$. In the experiment, we saw that this minimum occurred at a larger compressive strain of around -7% .

Figure 10 shows the results from the final viewing direction, where the structure was compressed along the e_3 direction, with c as the driving parameter and a as the orthogonal dimension. For this viewing direction, we present applied strains up to $\epsilon_c = -1.35\%$, because compressions beyond that are impossible in theory and might include breaking of the structure in the experimental tests. We see that the theoretical curve flattens off at $\epsilon_c = -1.35\%$, with an orthogonal strain of $\epsilon_a = -3.7\%$. In the experiment, we did not see this lateral contraction. Rather, there was little to no lateral deformation observed.

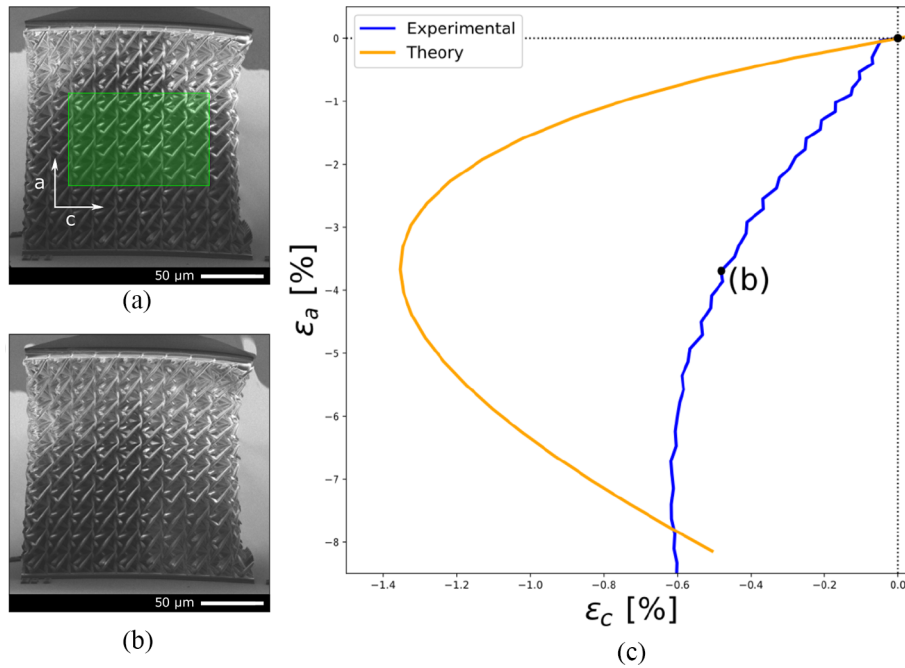


Figure 9. Strains and images from a compression test along the e_2 direction, measuring the orthogonal strain along c with a is the driving parameter. (a) The undeformed state of the structure. The analyzed region is highlighted in green and the directions a and c are indicated. (b) The deformed state at the end of the calculated auxetic interval.

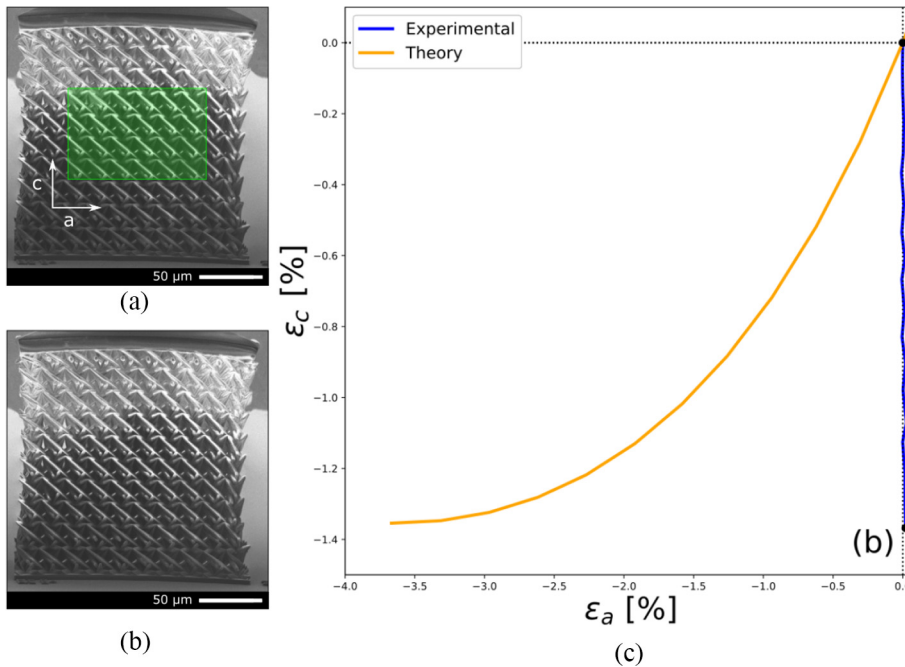


Figure 10. Strains and images from a compression test along the e_3 direction, measuring the orthogonal strain along a with c as driving parameter. (a) The undeformed state of the structure. The analyzed region is highlighted in green and the directions a and c are indicated. (b) The deformed state at the end of the calculated auxetic interval.

In the images for all three measurements, we can see that the strains in the structures are not evenly distributed. In particular, in the images of Figure 8, we see that the center of the structure contracts substantially more than the regions at the top and bottom of the structure.

5. Discussion

When the structure is compressed along the e_2 direction, with a as the driving parameter, the structure shrinks laterally under increasing compression in both perpendicular directions for the complete calculated auxetic interval. In the measurements, the calculated auxetic interval lies between the points (a) and (b).

Outside of the calculated auxetic interval, we see that the orthogonal a direction keeps shrinking with increasing load, while the c direction starts to expand again after an applied strain of -7% . This transition indicates the end of the auxetic interval and occurs later than was calculated from the theoretical model. For both directions, the orthogonal deformations are smaller than those resulting from theory. However, one must take into consideration that the theoretical model assumes unrestricted relative rotations at all joints while monolithic samples have limitations in this respect and introduce boundary conditions. In particular, the horizontal constraints introduced by the plates at the top and the bottom of the structure has had a visible effect on the deformation. This can be observed in Figure 8, where the center part of the structure contracts substantially more than the sides.

Overall, we observe that the nature of the deformation agrees with the geometric model. As the structure demonstrated no lateral expansion for each of the three orthogonal views of the structure, we have validated auxetic behavior over the calculated interval admitting compression.

6. Conclusion

In this study, we have shown that a framework design based on a geometric theory of periodic auxetics allows for a very explicit and precise description of its global periodic deformation. Furthermore, we have shown that such a framework can be produced using existing additive manufacturing technology at the micrometer scale. Compression tests have been performed on the manufactured frameworks and measurements confirm the auxetic behavior in the interval calculated using the theoretical model.


We emphasize the distinctive role of periodic framework designs with one degree of freedom. In the presence of several degrees of freedom, additional controls or constraints would be needed for selecting an auxetic deformation trajectory from response possibilities which definitely include non-auxetic deformations. Thus, the existence of a general methodology for one degree of freedom auxetic design is particularly relevant [40, 42]. The framework design considered here is of the simplest kind, in view of the fact that it has just two orbits of vertices under periodicity. Moreover, the presence and preservation of the four-fold symmetry allows explicit and precise computations.


Our investigation highlights the importance of predicting and recognizing the interval where auxetic behavior occurs. Within the class of one-degree-of-freedom periodic designs, the *volume increase factor* for the unit cell at the endpoints of the auxetic interval, provides a comparison criterion for auxetic performance.

Funding

This work was supported by National Science Foundation (award no.1704285 to C.S.B. and award no.1703765 to I.S.). At TU Delft, the project was part of the Nanoscience Engineering Research Initiative (www.tudelft.nl/neri).

ORCID iDs

Ciprian S. Borcea,  <https://orcid.org/0000-0002-6207-9127>

Freek Broeren,  <https://orcid.org/0000-0002-0564-2163>

References

- [1] Love, A. *A Treatise on the Mathematical Theory of Elasticity*. New York: Dover Publications, 1944.
- [2] Gibson, LJ, Ashby, MF, Schajer, GS, and Robertson, CL. The mechanics of two dimensional cellular solids. *Proc Roy Soc Lond* 1982; 382: 25–42.
- [3] Kolpakov, AG. Determination of the average characteristics of elastic frameworks. *J Appl Math Mech* 1985; 49(6): 739–745 (Engl. transl.); *Prikl Mat Mekh* 1985; 49 (6): 969–977 (in Russian).
- [4] Almgren, RF. An isotropic three-dimensional structure with Poisson's ratio = -1 . *J Elasticity* 1985; 15: 427–430.
- [5] Lakes, R. Foam structures with a negative Poisson's ratio. *Science* 1987; 235: 1038–1040.
- [6] Evans, KE, Nkansah, MA, Hutchinson, IJ, and Rogers, SC. Molecular network design. *Nature* 1991; 353: 124–125.

- [7] Sigmund, O. Tailoring materials with prescribed elastic properties. *Mech Mater* 1995; 20: 351–368.
- [8] Evans, KE, and Alderson, A. Auxetic materials: Functional materials and structures from lateral thinking! *Adv Mater* 2000; 12: 617–628.
- [9] Greaves, GN, Greer, AL, Lakes, R, and Rouxel, T. Poisson's ratio and modern materials. *Nat Mater* 2011; 10: 823–837.
- [10] Prawoto, Y. Seeing auxetic materials from the mechanics point of view: A structural review on the negative Poisson's ratio. *Computat Mater Sci* 2012; 58: 140–153.
- [11] Saxena, KK, Das, R, and Calius, EP. Three decades of auxetics research: Materials with negative Poisson's ratio: A review. *Adv Eng Mater* 2016; 18(11): 1847–1870.
- [12] Bertoldi, K. Harnessing instabilities to design tunable architected cellular materials. *Annu Rev Mater Res* 2017; 47: 51–61.
- [13] Lakes, RS. Negative-Poisson's-ratio materials: Auxetic solids. *Annu Rev Mater Res* 2017; 47: 63–81.
- [14] Kolken, HMA, and Zadpoor, AA. Auxetic mechanical metamaterials. *RSC Adv* 2017; 7: 5111–5129.
- [15] Ren, X, Das, R, Tran, P, Ngo, TD, and Xie, YM. Auxetic metamaterials and structures: A review. *Smart Mater Struct* 2018; 27: 023001.
- [16] Reis, PM, Jaeger, HM, and van Hecke, M. Designer matter: A perspective. *Extreme Mech Lett* 2015; 5: 25–29.
- [17] Kadic, M, Milton, GW, van Hecke, M, and Wegener, M. 3D metamaterials. *Nat Rev Phys* 2019; 1: 198–210.
- [18] Mirzaali, MJ, Pahlavani, H, and Zadpoor, AA. Auxeticity and stiffness of random networks: Lessons for the rational design of 3D printed mechanical metamaterials. *Appl Phys Lett* 2019; 115(2): 021901.
- [19] Askari, M, Hutchins, DA, Thomas, PJ, et al. Additive manufacturing of metamaterials: A review. *Additive Manuf* 2020; 36: 101562.
- [20] Zhang, J, Lua, G, and You, Z. Large deformation and energy absorption of additively manufactured auxetic materials and structures: A review. *Composites Part B* 2020; 201: 108340.
- [21] Bertoldi, K, Vitelli, V, Christensen, J, and van Hecke, M. Flexible mechanical metamaterials. *Nat Rev Mater* 2017; 2: 17066.
- [22] Grima, JN, and Evans, KE. Auxetic behaviour from rotating squares. *J Mater Sci Lett* 2000; 19: 1563–1565.
- [23] Mitschke, H, Schwerdtfeger, J, Schury, F, Stingl, M, et al. Finding auxetic frameworks in periodic tessellations. *Adv Mater* 2011; 23: 2669–2674.
- [24] Elipe, JCA, and Lantada, AD. Comparative study of auxetic geometries by means of computer-aided design and engineering. *Smart Mater Struct* 2012; 21: 105004.
- [25] Mitschke, H, Schury, F, Mecke, K, Wein, F, Stingland, M, and Schröder-Turk, GE. Geometry: The leading parameter for the Poisson's ratio of bending-dominated cellular solids. *Int J Solids Struct* 2016; 100: 1–10.
- [26] Lim, T-C. Analogies across auxetic models based on deformation mechanism. *Phys Stat Solidi* 2017; 11(6): 1600440.
- [27] Wells, AF. The geometrical basis of crystal chemistry. *Acta Cryst* 1954; 7: 535.
- [28] Wells, AF. *Three Dimensional Nets and Polyhedra*. New York: Wiley, 1977.
- [29] Delgado-Friedrichs, O, and O'Keefe, M. Identification of and symmetry computation for crystal nets. *Acta Cryst A* 2003; 59: 351–360. (doi:10.1107/S0108767303012017)
- [30] Sunada, T. *Topological Crystallography*. Berlin: Springer, 2013.
- [31] Dove, MT. Theory of displacive phase transitions in minerals. *Amer Mineral* 1997; 82: 213–244.
- [32] Borcea, CS, and Streinu, I. Periodic frameworks and flexibility. *Proc Royal Soc A* 2010; 466: 2633–2649.
- [33] Dove, MT, and Fang, H. Negative thermal expansion and associated anomalous physical properties: Review of the lattice dynamics theoretical foundation. *Rep Prog Phys* 2016; 79: 066503.
- [34] Yeganeh-Haeri, A, Weidner, D, and Parise, J. Elasticity of α -cristobalite: A silicon dioxide with a negative Poisson's ratio. *Science* 1992; 257: 650–652.
- [35] Grima, JN, Jackson, R, Alderson, A, and Evans, KE. Do zeolites have negative Poisson's ratios? *Adv Mater* 2000; 12: 1912–1918.
- [36] Siddorn, M, Coudert, F-X, Evans, KA, and Marmier, A. A systematic typology for negative Poisson's ratio materials and the prediction of complete auxeticity in pure silica zeolite JST. *Phys Chem Chem Phys* 2015; 17: 17927–17933.
- [37] Dagdelen, J, Montoya, J, de Jong, M, and Persson, K. Computational prediction of new auxetic materials. *Nat Commun* 2017; 8: 323.
- [38] Borcea, CS, and Streinu, I. Geometric auxetics. *Proc R Soc A Math Phys Eng Sci* 2015; 471: 20150033.
- [39] Borcea, CS, and Streinu, I. New principles for auxetic periodic design. *SIAM J Appl Algebra Geom* 2017; 1: 442–458.
- [40] Borcea, CS, and Streinu, I. Periodic auxetics: Structure and design. *Q J Mech Appl Math* 2018; 71: 125–138.
- [41] Borcea, CS, and Streinu, I. Auxetic regions in large deformations of periodic frameworks. In: Kecskeméthy, A, Flores, FG, Carrera, E and Elias, DA (eds) *Interdisciplinary Applications of Kinematics* New York: Springer, 2019, pp. 197–204.
- [42] Borcea, CS, and Streinu, I. Auxetics abounding. In: *Proceedings 4th IEEE/IFTOMM International Conference on Reconfigurable Mechanisms and Robots*, Delft, the Netherlands, June 2018, pp. 20–22.
- [43] Liu, Y, Campbell, JH, Stein, O, Jiang, L, Hund, J, and Lu, Y. Deformation behavior of foam laser targets fabricated by two-photon polymerization. *Nanomaterials* 2018; 8(7): 498.
- [44] Farnebäck, G. Two-frame motion estimation based on polynomial expansion. In: Bigun, J and Gustavsson, T (eds.) *Image Analysis*. Berlin: Springer, 2003, pp. 363–370.
- [45] Bradski, G. The OpenCV Library. *Dr. Dobb's J Softw Tools*. Nov 2000, 25(11): pp.120, 122–125.